# New Insight into the Wax Precipitation Process: In Situ NMR Imaging Study in a Cold Finger Cell

Evgeny V. Morozov,*,[†,‡,§] Oleg V. Falaleev,[||] and Oleg N. Martyanov*,[§]

[†]Kirensky Institute of Physics, Siberian Branch of the Russian Academy of Sciences, Akademgorodok 50/38, Krasnoyarsk 660036, Russia

[‡]Institute of Chemistry and Chemical Technology, Siberian Branch of the Russian Academy of Sciences, Akademgorodok 50/24, Krasnoyarsk 660036, Russia

[§]Boreskov Institute of Catalysis, Siberian Branch of the Russian Academy of Sciences, Pr. Ak. Lavrentieva 5, Novosibirsk 630090, Russia

[||]Krasnoyarsk Scientific Centre, Siberian Branch of the Russian Academy of Sciences, Akademgorodok 50, Krasnoyarsk 660036, Russia

**ABSTRACT:** A cold finger cell intended for the wax deposition measurements was fabricated and integrated into an NMR imaging probe for the noninvasive study of wax precipitation processes in situ. The cell was first tested with a model system; then, a series of experiments with different thermal gradients applied to the cell were performed for a waxy crude oil. NMR imaging of the operating cell revealed the formation of a deposit with the morphology and dynamics strongly correlating with the temperature regime. At higher temperatures of cold finger, the incipient wax gel ages uniformly, giving rise to the hard and thin inner layer of deposit accompanied by a branched loosely consolidated outer layer. Conversely, the lower temperatures facilitate formation of a thick deposit which no longer ages uniformly and slow down the diffusion-controlled growth of the branched deposit structure. The results obtained are consistent with the majority of the data previously reported. Thus, gelation of the wax at temperatures below the cloud point and subsequent thermal-driven diffusion processes are considered to be the dominant mechanisms of the deposit formation. The counter diffusion and Ostwald ripening aging concepts were found to be relevant in the case of the cold finger study and account for the phenomena observed in this work. The information obtained via NMR imaging is highly complementary to the results obtained by other techniques that can aid in understanding the essential processes behind the wax precipitation phenomena. The approach developed can be effectively extended to study any thermal-driven phase separation process.

## 1. INTRODUCTION

Phase separations which take place during various chemical processes in many systems play a crucial role in industry and related technologies. Such relevant processes as precipitation, crystallization, flocculation, gelation, etc. result in the formation of particular phases in complex systems. Mostly the phase separation is a predetermined and very controllable process involved in a particular technology, but it can also be a great challenge in such cases as fouling of heat-transfer components and pipelines.[1] The most severe and economically costly problems associated with phase separation lie in the area of crude oil production, transportation, and processing. Crude oil is a well-known complex mixture of hydrocarbons consisting of paraffins, aromatics, naphthenes, resins, and asphaltenes.[2,3] Among these groups of hydrocarbons, high molecular weight paraffins (waxes) and asphaltenes are responsible for some of the problems occurring during the transportation and processing of crude oil. While asphaltenes contribute mostly to the problems associated with oil refining and processing,[4] the wax deposition on the walls of reservoirs and pipelines causes the increased pressure drop, decreased efficiency, and eventual blockage followed by pipe damage.[5] The temperature of the wax crystal appearance in crude oil is referred to as the cloud point or wax appearance temperature (WAT).[6] The gelling of crude oils at temperatures below WAT can lead to significant non-Newtonian behavior and increase in the effective viscosities

of waxy crude oils which is actually a great challenge for oil production in rather cold regions or in deep-sea environments.[7] Solidified waxes in diesel fuel can also clog the fuel filters and injectors in engines, leading to serious energy and material losses. In particular, the changes of the cloud point with the pressure increase must be taken into account, for example, in the development of new diesel engines where diesel is injected under high pressure.[8] It is clear that the prevention of wax formation in different processes requires deep understanding of the behavior of the paraffin molecule crystallization at certain temperatures and pressures. Hence the challenges associated with the wax deposition have great relevance and deserve close consideration.[5,7,9]

Generally wax is considered as a mixture of long-chain hydrocarbons with a broad distribution of carbon numbers, ranging from C18 up to C100+.[10] These hydrocarbons are less soluble in crude oil at lower temperatures and tend to crystallize and deposit on cooler surfaces when the crude oil is subjected to a colder environment. The crystallization of paraffins leads to the formation of a gel network with a complex morphology; the latter is greatly affected by the wax composition, process conditions, and time.[11] A number of

mechanisms have been proposed to elucidate the wax deposition process. These mechanisms include molecular and Brownian diffusion, gelation, gravity settling, thermodiffusion (Soret effect) and thermophoresis, shear dispersion, Saffman effect, shear removal (stripping and prevention), etc.[5,7,9,11−13] It is generally believed that a thorough understanding of the mechanisms behind the wax deposition will enable researchers to predict the formation and evolution of a wax layer, allowing the development of additives and surface treatments to be more successful in hindering wax deposition within pipelines.[14]

Many experimental studies complemented by comprehensive modeling have been carried out to gain an insight into the deposition mechanisms. Most of them deal with the laboratory-scale experiments performed both under static and dynamic conditions and intended to reveal the impact of different factors on the wax deposit formation.[15] The mass of the deposit and its thickness were detected and measured depending on the temperature, pressure, and flow rate.[9,16−20] The easiest and most popular way to estimate the mass/thickness of the deposit is a direct measurement (pigging or "take out" method[5]) combined with ex situ chemical and microscopic analysis of the extracted wax.[19] However, this approach is quite invasive and cannot be successfully applied in many cases. Consequently, various techniques have been developed for indirect real-time measurements of the wax deposit layer, such as pressure drop measurements,[20] laser-based techniques,[20,21] polarized optical microscopy,[22] X-ray diffraction,[14] liquid displacement-level detection,[23] acoustic[24] and ultrasound-based techniques,[25] temperature modulated differential scanning calorimetry,[26] heat pulse wax monitoring,[27] electrical capacitance tomography[28] etc.[29,30] Despite the evident advantages of these methods in providing the information on the deposit thickness evolution with time and great efforts spent for studying the correlations between the properties of crude oils and their flowing properties, there is still a lack of knowledge about some aspects of deposit layer structure and morphology.[31,32] The intensively modeled[33] temperature distribution inside the deposit can hardly be evaluated as well. So far, further understanding of the wax precipitation and deposition mechanisms is still needed.

A promising approach and an essential step in this direction is the application of modern techniques in situ.[34−36] The in situ regime is needed to elucidate and separate the factors influencing the wax precipitation and determine the mechanism of deposits formation. To address some of these problems, the NMR imaging (MRI) method has been applied in this study for in situ measurements of the deposit formation. The main advantages of MRI stem from the fact that the NMR signal is very sensitive to any small alterations of the chemical composition, physical structure, and temperature in the systems under study. Thus, MRI being a well-known noninvasive visualization technique has been successfully applied in many areas of research such as materials science, chemical engineering, petroleum science, etc.[37−39] Recently, NMR imaging has been demonstrated to be an informative tool for studying the phase behavior in crude oils.[40−43]

To simulate the wax deposition in pipelines, two different types of laboratory devices are commonly employed: flow loops and cold finger. While the flow loop seems more natural in the sense of the simulation in pipelines, the cold finger device is much simpler for implementation. At the same time the results achieved via the cold finger cell revealed their high significance associated with the remarkable predictive capacity.[44−50] For this

reason we decided to employ the cold finger device for in situ measurements, and the first aim of the study was to develop a cold finger cell combined with the NMR imaging probe. The developed methodology was expected to provide a general approach for investigating any kind of thermal-driven phase separation processes, including wax precipitation. After the method validation, the second objective was a noninvasive real-time study of the wax precipitation from natural crude oil.

## 2. EXPERIMENTAL SECTION

**2.1. Samples.** To validate the method, glycerol as a model system was used first (≥99.5% purity, purchased from Sigma-Aldrich). The visualization of the wax deposition was carried out using the crude oil originated from the eastern oilfield of Mongolia.[51,52] The composition of this waxy oil is summarized in Table 1. The chemical composition

**Table 1. Composition of the Crude Oil Sample (Eastern Oilfield of Mongolia)**

| component | content, % mass |
|---|---|
| asphaltenes | 0.22 |
| N-alkanes | 18.01 |
| wax solid ($C_{17}$–$C_{38}$) | 11.12 |
| resins | 14.7 |
| elements | |
| C | 86.46 |
| H | 13.28 |
| N | 0.14 |
| O | 0.06 |
| S | 0.06 |

of the oil was determined according the procedure developed earlier for the waxy oils.[52,53] The method used for the asphaltenes extraction in this case repeats the ASTM method D6560-005.[54] The pour point and the wax appearance temperature of the oil were 29 and 44 °C, respectively. The pour point was determined according to ASTM method D97.[55] The WAT was determined using the temperature dependence of oil viscosity: a plot of natural log of viscosity versus inverse of temperature gives the point at which a remarkable change of slope occurs.

This method provides reasonable accuracy of the measurements.[56] Nevertheless, WAT was separately confirmed using NMR imaging: wax agglomerates with size >0.1 mm are clearly visible on the images in the form of dots with low signal intensity when the temperature of the oil is below WAT. Consequently, the temperature when the oil becomes homogeneous on the NMR images corresponds to WAT. Numerous tests reveal this temperature to be 44 ± 2 °C, which is very consistent with the value determined via viscosity measurements. The viscosity and the density of the crude oil at different temperatures were measured by a viscosimeter SVM 3000 (Anton Paar GmbH, Austria) following ASTM method D7042[57] and shown in Figure 1.

Crude oils originated from the eastern oilfield of Mongolia have attracted significant attention in the last two decades because these oils have relatively low amount of sulfur and heavy metals, making the refining processes much easier.[58,59] However, the oils are paraffinic, which leads to some problems with their transportation and storage. Because the Mongolian oil has high practical importance and is suitable for meeting the objectives of this study, it was decided to investigate this oil first.

**2.2. Cold Finger Cell.** To investigate the wax deposition in situ, a special removable cold finger cell was designed and fabricated. The basic idea of the cold finger cell is rather common and can be found in previous studies.[44−50] The only difference is that the stainless steel elements were replaced by glass and plastic to avoid magnetic field distortion inside the warm bore of superconducting magnet. The scheme of the cell is illustrated in Figure 2. The cold finger cell consists of two long coaxially aligned tubes passing through the entire
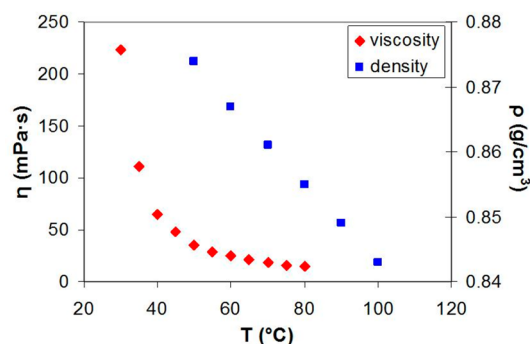
**Figure 1.** Temperature dependencies of the viscosity and density of the Mongolian oil sample.
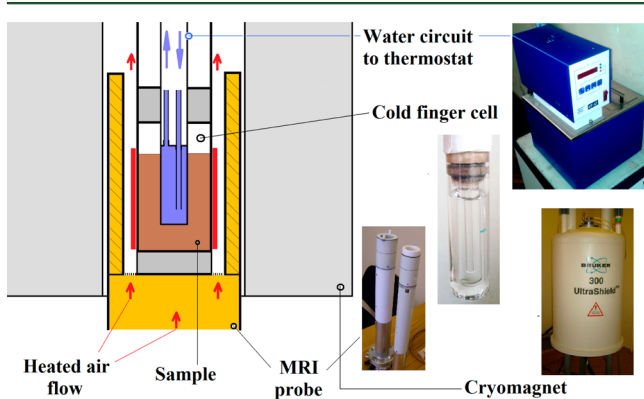


**Figure 2.** Scheme of the experimental setup: the cold finger cell mounted into the MRI probe.

length of the magnet bore: the inner glass tube is placed inside the outer plastic tube and tightly fixed there with fluoroplastic and rubber spacers. This inner tube is closed and connected with the thermostat (VT 10-2, TERMEX Ltd.) by rubber pipes to provide circulating of the coolant (water) inside; i.e., this inner tube is a coldfinger. On the end of outer plastic tube, the glass removable ampule is tightly attached, forming a sealed bath around the cold finger. Into this bath the sample is poured for investigation. Before the experiment the assembled cell with the poured sample inside is inserted into the warm bore through the upper hole and appears in the MRI probe. The temperature of the inner wall of the bath (cold wall) is maintained by water cooling with ±1 °C accuracy, whereas the temperature of the outer wall of the bath (warm wall) is maintained by heated air flow provided by a standard temperature/flow unit of a Bruker AVANCE DPX NMR spectrometer. The spectrometer automatically controls the output flow speed of heated air and its temperature with ±0.5 °C accuracy. The 400−800 L/h flow rates were used, which provided uniform and stable heating of the cell. Thermal control of the walls inside the cell allowed maintaining the sample under the prescribed thermal gradient. To decrease the effects of nonuniform heating, the bottom of the cold finger cell was thermally isolated by foam plastic, and the air flow was directed in such a way as to heat the walls only. The cell dimensions were as follows: $R_i$ − the radius of the inner tube, $R_e$ − the radius of the outer tube, $r_0$ − their difference $(R_e − R_i)$. Volume of the sample load was approximately 10 mL. The fabricated cell was supplied with the tubes of different diameters, making it possible to vary the $r_0$.

**2.3. MRI Method.** The NMR imaging method allows measuring the intensity of the NMR signal coming from the selected area of the sample (the detailed information on how MRI works can be found in refs 37, 38, and 60). Using MRI one can obtain either a 2D map of the signal intensity distribution, which is, in its turn, strongly correlated with the local spin−lattice ($T_1$) and spin−spin ($T_2$) relaxation times, or directly a 2D map of the $T_1$, $T_2$ distribution itself. The relaxation

time depends on different parameters of the system such as density, composition, structure, viscosity, flow speed, diffusion coefficient, temperature, etc., because these parameters affect the correlation time of the fluctuating local magnetic field via different mechanisms.[61] When the system is complex and contains many different constituents (such as crude oil), the resulting relaxation rate is a superposition of all the relaxation components in the system according to their partial weights: $1/T_2 = N_1[1/T_2^1] + N_2[1/T_2^2] + ... + N_n[1/T_2^n]$, where $N_n$ is the partial weight of the relaxation component with $T_2^n$, and which is, in its turn, related to the concentrations of the appropriate constituent. So, the phase separation processes in the system affect the relaxation times and/or their weights, changing the NMR signal. Consequently, the MRI method is highly sensitive to a small alteration of the system parameters. Typically, the most sensitive parameter contributing to the eventual signal variation on the NMR images is the spin−spin relaxation time $T_2$. To have an informative picture we can adjust the NMR image contrast by changing the range of measuring relaxation time $T_2$ where it mostly depends on the parameter analyzed, while all other parameters contributing to the signal are diminished. One can do it easily just by changing the instrumentation parameters.

The MRI experiments were carried out using an NMR imaging installation based on a Bruker AVANCE DPX 200 console and a superconducting magnet with an 89 mm diameter vertical bore, water-cooled and self-shielded Bruker gradient set (maximum gradient strength up to 292 mT/m); probe PH MINI 0.75, 38 mm internal diameter birdcage coil tuned and matched to 1H nuclear resonance frequency of 200.13 MHz; and a console operated with Paravision 4.0 software.

Transverse slice selective 2D NMR images were acquired using the spin−echo-based pulse sequence supplied by the imager software: $T_2$-weighted images were acquired by the multi slice multi echo (MSME) technique;[62] $T_2$ maps were plotted by processing the image sequences acquired by the same technique (using the standard Image Sequence Analysis option). The image acquisition parameters were as follows (unless otherwise mentioned in the figure captions): slice thickness (Sl) of 1 mm; field of view (FOV) of 40 mm; matrices of 256 × 256 pixels. The repetition time (TR) and echo time (TE) were adjusted depending on $T_1$ and $T_2$ of the sample to provide the best contrast. The time of the image acquisition (TA) depended on the TR and TE parameters, and the number of scans was maintained as short as possible; the number of echoes for the MSME technique was 28. The spatial $T_2$ profiles were evaluated by plotting $T_2$ vs the coordinate corresponding to the pixel position on the $T_2$ map.

**2.4. Experimental Procedure and in Situ Method Validation.** The first aim when testing the cold finger cell was to prove the presence of the steady temperature gradient in the model sample during the cell exploitation. Ideally, the model sample should be a liquid with reasonably high viscosity to restrict thermal convection and avoid significant mass transfer during the long time of cell operation. Apparently, the most suitable substance to be chosen was glycerol. It has high temperature-dependent viscosity which provides the high sensitivity of NMR relaxation times to small temperature variations. Glycerol $T_1$ and $T_2$ temperature dependencies were measured in an MRI probe by routine NMR spectroscopy methods (inversion−recovery and CPMG pulse sequences[60−62] for $T_1$ and $T_2$, respectively) in a common glass tube before the experiments in the cold finger cell and presented in Figure 3. By assuming the steady state and time-independent temperature, the thermal profile between the cold and warm walls in the cell satisfies the following equation:[46]

$$T(r) = T_i + \frac{(T_e − T_i)}{\ln \frac{R_e}{R_i}} \ln \frac{r}{R_i}$$

(1)

where $T_i$ is the temperature of the internal wall, $T_e$ is the temperature of the external wall; $R_i$ and $R_e$ are the radii of the cold finger and outer tube, respectively. Thus, in the static case eq 1 gives a well-known logarithmic dependence.

The in situ MRI visualization of the operating cold finger cell apparently demonstrates the emerging thermal gradient along the radius (the $T_2$-weighted NMR image of the cell with glycerol is
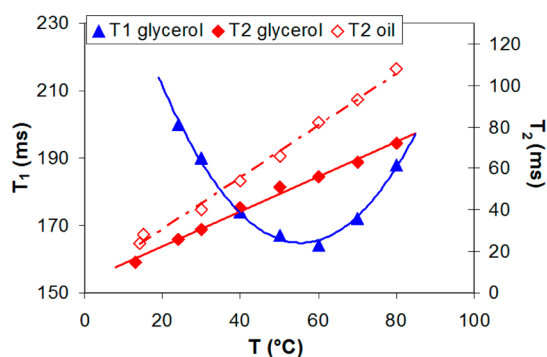
**Figure 3.** Glycerol ($T_1$, $T_2$) and Mongolian oil ($T_2$) temperature dependencies measured in common NMR tube using inversion−recovery (for $T_1$) and CPMG (for $T_2$) pulse sequences.

inferred from these images. The signal intensity on the $T_2$-weighted image acquired using the MSME technique follows the equation:[60,62]

$$I \propto \rho \left[ 1 - \exp\left( \frac{TE - TR}{T_1} \right) \right] \exp\left( \frac{-TE}{T_2} \right) \qquad (2)$$

where $\rho$ is the proton density, and all other parameters are introduced in section 2.3. By considering the proton density to be independent on the coordinate and taking into account the known image parameters (TR and TE), it is possible to theoretically evaluate $I(r)$ profiles based on the prescribed thermal profiles and compare them with those measured experimentally. This was done as follows: using the actual T-profiles (Figure 5a), $T_1$, $T_2$ dependencies (Figure 3) and parameters TR, TE equal to those used in the experiments, the $I(r)$ profiles were calculated (by means of eq 2) along the radius and then, normalized with respect to the first point, Figure 5b. As is seen, the experimental data are very consistent with the calculated curves. It means that either $T_2$-maps or $T_2$-weighted images visualize the thermal gradient in the cell quite well, and the cell itself is feasible and provides the prescribed thermal gradient.

In contrast to the model system, the temperature variation in crude oil between the warm and cold walls may cause wax precipitation if the temperature appears lower than WAT. Consequently, wax precipitation changes the composition of the oil. Yet, the relaxation behavior of the crude oil is very complex: plenty of constituents produce complicated relaxation decay with many components, each of them depending on temperature in its specific way. All these complexities discard the necessity in a special calibration of $T_2$ with the temperature similar to those described above for glycerol, because even small composition changes result in a noticeable distortion of the initial calibration curve.

Despite the complexity, the apparent temperature dependence of the relaxation time $T_2$ appears linear (the graph is presented in Figure 3). However, the MRI visualization can be focused on the $T_2$-maps and $T_2$-weighted images regardless of the necessity of their converting into the T-map: the in situ methodology validated using the model sample has already proven the presence of the prescribed thermal gradient. Examples of the $T_2$-maps with appropriate $T_2$-profiles of the cell with oil are presented in Figure 6. The temperatures of cold/warm walls were 15/30 °C and 15/40 °C for the left and right images, respectively. The cell dimensions were $R_i$ = 5.9 mm, $R_e$ = 15.2 mm, $r_0$ = 9.4 mm; in this experiment the distance $r_0$ was increased as compared to those used in experiments with glycerol to decrease the thermal gradient and slow down the mass transfer. The thermal gradient was switched on for a short period of time (0.5 h); this time is significantly shorter than those required for a noticeable changing of oil composition along the radius at present conditions (typically, it takes about 10−14 h). Thus, the profiles demonstrated are steady and remain unchanged during 10−14 h after the beginning of the experiment.
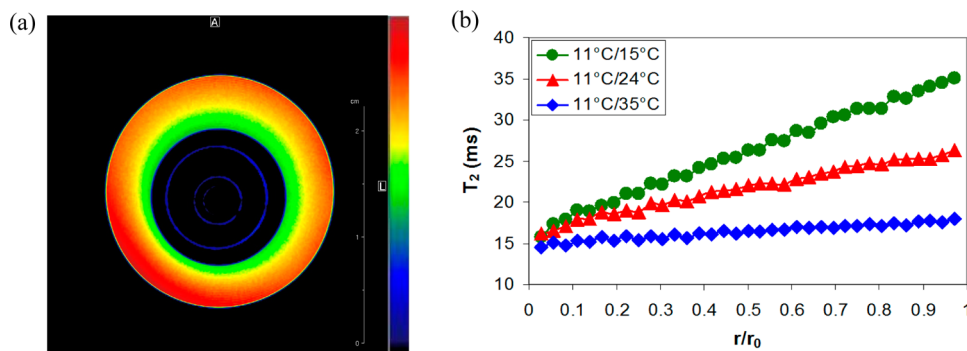
presented in Figure 4a). The stream of water flowing through the pipes was not visible on the images: despite the inherently high value of $T_2$, the protons encoded by the slice selective magnetic field gradient are leaving the image slice too fast to be detected during the readout, making the apparent $T_2$ extremely low (only the thin layer of the water in the vicinity of the walls could be slightly detectable). To evaluate the temperature distribution within the cell, a series of $T_2$ maps were acquired for different prescribed temperatures of the cold/warm walls. The resulting radial $T_2$-profiles are presented in Figure 4b, where the temperatures of the cold and warm walls are referred to as $T_i/T_e$, namely, 11 °C/15 °C, 11 °C/24 °C, and 11 °C/35 °C. The cell dimensions were as follows: $R_i$ = 6.3 mm, $R_e$ = 10.6 mm, $r_0$ = 4.3 mm. Thus, within the gap of 4.3 mm the relatively small temperature gradients (the highest among of them was approximately 5.6 deg °C/mm) provide high glycerol viscosity and guarantee that no convective motions could have been induced inside the cold finger cell.

The smallest temperature difference (only 4 °C) was intended to test the sensitivity of the visualization technique. Higher thermal gradients could result in faster mass transfer, but the tendency to speed up the process is counterbalanced by the necessity to keep the conditions of pure thermal conductance. On the basis of practical experience and previous observations[45,49,63] to set the temperatures of the cold and warm walls about WAT ± 10 °C is enough for deposition experiments. For this reason the largest temperature difference was prescribed to be 24 °C, Figure 4b. Using the dependence of $T_2$ on temperature (Figure 3), the $T_2$-profiles presented in Figure 4b were turned into the T-profiles and then were compared with those predicted theoretically according to eq 1, Figure 5a. As can be seen, good agreement between the measured and predicted T-profiles was observed for the model system that additionally confirms pure thermal conductance regime.

Despite the sufficient quality of the $T_2$-maps used in MRI, the sensitivity and the contrast were much higher when using the $T_2$-weighted images. However, the temperature could not be directly



**Figure 4.** $T_2$-weighted NMR image of the operating cold finger cell with glycerol (a); the image parameters are TR = 1200 ms, TE = 20 ms, FOV = 3.2 cm, Sl = 2 mm. Series of radial $T_2$-profiles with different temperatures of cold and warm walls (b).
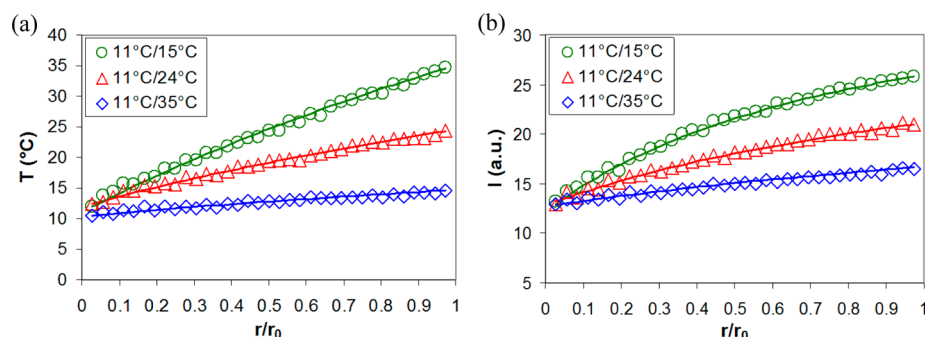
**Figure 5.** Experimental temperature (a) and signal intensity (b) profiles (symbols) superimposed on the appropriate theoretical profiles (solid lines).
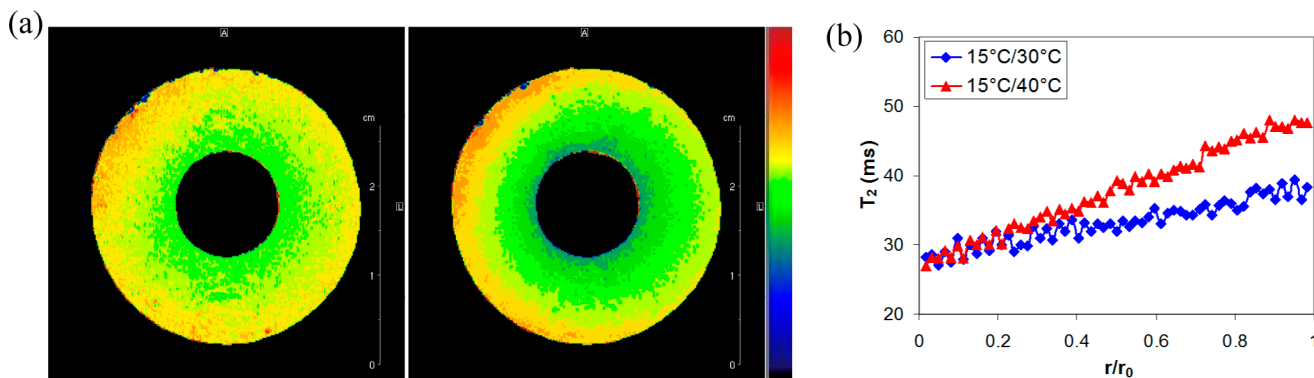


**Figure 6.** $T_2$-maps of the operating cold finger cell with the Mongolian crude oil (a); the image parameters are FOV = 4 cm, Sl = 2 mm, color bars are scaled differently for every image. Two appropriate radial $T_2$-profiles with different temperatures of cold/warm walls (b).
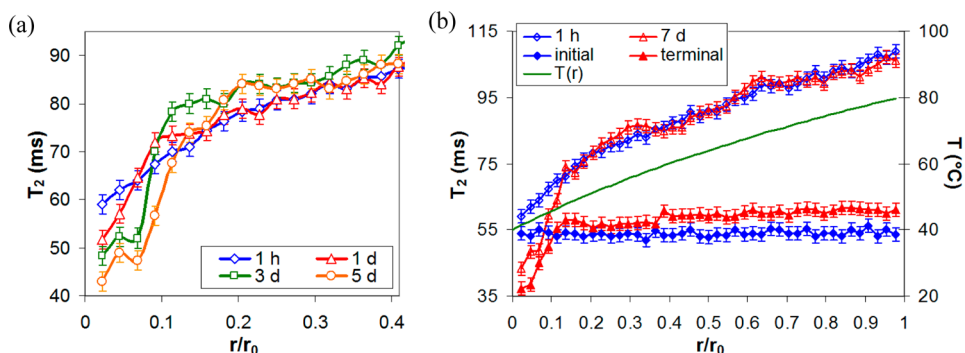


**Figure 7.** Radial $T_2$-profiles of the cold finger cell with Mongolian crude oil sample. Panel (a) demonstrates the evolution of the $T_2$-profiles within $r/r_0 < 0.4$ zone; panel (b) shows relaxation profiles at the beginning and at the end of experiment.

## 3. RESULTS AND DISCUSSION

Preliminary experiments with glycerol and oil samples during testing of the cold finger cell demonstrate fast emerging of the thermal gradients inside the cold finger cell just after beginning of the experiment (less than in 10 min). Since 30 min the gradients are steady for as long as studied (glycerol), and steady during the time until the deposition processes change the composition of the sample (crude oil). It was clearly detected by tracking the relaxation profiles evolution with time: once having achieved the steady state, the profiles remain unchanged.

In the first series of long time experiments, the temperatures of the cold and warm walls were set to 40 and 80 °C, respectively. When the oil has been melted and poured into cold finger cell, the whole cell including cold finger surface was heated up to 50 °C for homogenizing and erasing any thermal history of the oil sample; meanwhile the cooling had not been switched on yet. After sample homogenizing, the cooling was

switched on and the temperature of the cold finger was decreased to 40 °C, while the temperature of the air flow was increased to 80 °C, yielding the prescribed temperature gradient.

The $T_2$-maps acquired during operation of the cold finger cell reveal evolution of the $T_2$-profiles. During the first 6−8 h after beginning no significant change was observed, but then the relaxation times in the vicinity of the cold wall started to decrease, Figure 7a. This process was accompanied by slow spreading of this "low $T_2$" zone during 7 days of experiment. In Figure 7b the relaxation profiles in the beginning and after 7 days of experiment are presented for comparison, where "1h" and "7d" denote relaxation profiles recorded during cell operating, i.e., while the temperatures of cold finger and warm wall in the cell were 40 and 80 °C, respectively. The profile obtained before the heating has been switched on is denoted as "initial", while the profile obtained after 7 days of
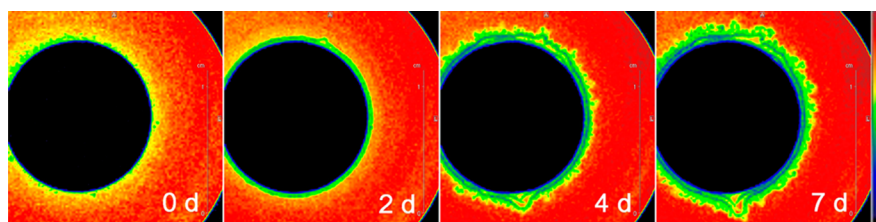
**Figure 8.** Series of the $T_2$-weighted images of the cold finger cell with the Mongolian crude oil sample during cell operating with cold/warm wall temperatures of 40/80 °C; parameters of pulse sequence: TR = 2500 ms, TE = 50 ms.
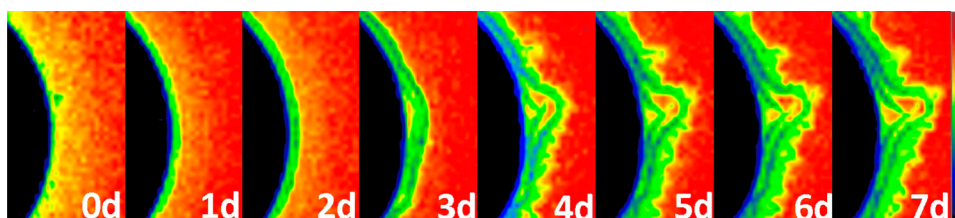


**Figure 9.** Evolution of the particular deposit region of the cold finger cell; the parameters are the same as indicated in Figure 8.

experiment when the heating has been already switched off is denoted as "terminal"; i.e., both these profiles were recorded when no temperature gradient was applied, and the whole cell was at 40 °C. The cell dimensions were $R_i$ = 5.8 mm, $R_e$ = 12.6 mm, $r_0$ = 6.8 mm (the latter was reduced to avoid impact of well-known MRI artifacts, emerging in the vicinity of surface of birdcage radiofrequency coil). As can be seen, the resulting temperature gradient was approximately 5.9 deg °C/mm, which along with relatively high viscosity of waxy oil (Figure 1) should provide conditions for pure thermal conductance regime. The profiles in Figure 7 confirm that no convective motions have arisen. For convenience the theoretical T-profile (calculated according to eq 1 with assigned temperatures of the walls) is also presented in Figure 7b to show the initial temperature distribution inside the cell.

The detailed analysis of relaxation profiles presented in Figure 7 revealed the appearance of the regions which have their own characteristic $T_2$ values. The first region is $r/r_0 < 0.07$ with low and sharp $T_2$ = 37−38 ms, the second region is $0.07 < r/r_0 < 0.15$ with a broad distribution of $T_2$ = 39−55 ms, and the third region is $0.15 < r/r_0 < 0.4$ with $T_2$ = 56−58 ms (all relaxation times are inferred from the "terminal" profile recorded when no thermal gradient was applied). The remaining part of the oil sample, $r/r_0 > 0.4$, demonstrates characteristic $T_2$ = 60 ± 1 ms. Selection of the regions described is well confirmed by the "7d" profile recorded during cell operating (when the thermal gradient was still applied): there are pronounced changes of slope in corresponding points $r/r_0$ = 0.07, 0.15, and 0.4. According to NMR fundamentals, if two distinct parts of the system demonstrate different values of relaxation time $T_2$, these parts must be different in terms of their chemical composition and/or structure (when their temperatures are the same). Consequently, the major $T_2$ difference between the regions of $0 < r/r_0 < 0.15$ and $0.15 < r/r_0 < 1$ indicates their extremely distinct nature.

As it was mentioned in section 2.3, the apparent relaxation time $T_2$ is a sum of contributions which come from all types of protons in the system. Despite the similar chemical nature of the wax and major part of the oil constituents, their molecular weights are quite different. Generally, long chains of high molecular weight compounds such as paraffin demonstrate a relatively slow local dynamics and longer correlation times of the fluctuating local magnetic fields[61] as compared to the smaller molecules with shorter chains and faster segmental motion. According to the Bloembergen−Purcell−Pound (BPP) theory,[64] longer correlation times correspond to lower spin−spin relaxation times and vice versa. As a result, an apparent $T_2$ value evidently decreases as the concentration of heavy components with short $T_2$ increases.

However, the apparent relaxation time decreases not only due to an increase of the concentration of heavy components. When the initially homogeneous liquid turns into a colloid system (particularly, appearing of the wax crystals in the oil below WAT), the relaxation time declines dramatically due to the enormous increase of specific surface area of solids. It is well-known that any solid surface in the system is a perfect relaxant which speeds up the NMR relaxation: the magnetic field nearby the surface is always inhomogeneous, causing intensive dephasing of magnetization (shortening of $T_2$). Furthermore, the surface mechanically restricts the local motion of the molecules in the surrounding medium due to the shell appearing around colloid particles (restricted local motion causes $T_2$ shortening as well). All this results in a sufficient decrease of $T_2$ once the system becomes inhomogeneous.

Taking into account these considerations, appearance of the regions with different characteristic relaxation times $T_2$ in Figure 7 indicates the redistribution of the heavier components during cell operation. By comparing the "initial" and "terminal" profiles, one can conclude that the region $0 < r/r_0 < 0.15$ has to be considered as wax-enriched, while the remaining part of the oil $0.15 < r/r_0 < 1$ is wax-depleted, Figure 7b.

Additional information can be inferred from the analysis of the NMR images acquired simultaneously with the $T_2$-profiles. Figure 8 presents a series of images obtained during operation of the cold finger cell. The contrast scheme on the images was adjusted to provide $T_2$-weighting (the parameters of pulse sequence are listed in figure caption), which is the best suitable for careful deposit detection, meanwhile neglecting proper visualization of the thermal gradient itself. As can be seen, in the beginning of experiment the cold finger surface is clear, and then within 1 to 3 days the deposit starts and continues to grow with time and forms an initially even layer. But after some time the layer surface becomes rough with a large number of individual growth points which form a second deposit layer

9008

with a branched (irregular) structure. Apparently, these layers having a fine structure contain some amount of the entrapped oil and show weak adhesion to the wall and to each other.

A more detailed picture of deposit formation and evolution is presented in Figure 9 for the particular region close to the cold finger surface. Apparently the first deposit layer remains uniform within 3 days of experiment; at the same time the growing of the second layer and developing of the branched deposit-oil boundary only slightly affects its thickness and morphology.

The comparison of the deposit structure revealed by the NMR images with the $T_2$-profiles in Figure 7 shows that the solid deposit eventually occupies the region of $0 < r/r_0 < 0.15$, where the wax-enriched layer has been identified according to significantly lower values of relaxation time $T_2$. Furthermore, the regions $r/r_0 < 0.07$ with $T_2 = 37-38$ ms and $0.07 < r/r_0 < 0.15$ with $T_2 = 39-55$ ms evidently correspond to the first and second deposit layers. The difference between two layers is well confirmed either on the NMR images where they have a very distinct appearance, or on the relaxation profiles, where $T_2$ values are sharp for the uniform layer and are widely distributed over the thickness for the branched one. The region $0.15 < r/r_0 < 0.4$ with $T_2 = 56-58$ ms was not clearly visible on the NMR images most likely due to a very small $T_2$ difference (3−4 ms, whereas the error bars are ±2 ms) with the remaining part of the oil sample.

Among the different mechanisms which have been proposed to address the wax deposition process,[5,7,9,11−13] the diffusion-based mechanisms (such as molecular and Brownian diffusion, Soret effect) are the most relevant for the experiment in the cold finger cell, where the only static conditions are presented and gravity force is parallel to the deposition plane. Decreasing of the oil temperature below the WAT in the vicinity of the cold walls causes local system oversaturation, resulting in the wax precipitation. Consequently, the liquid phase concentration gradient of the dissolved wax arises and wax molecules start migrating toward the cold wall. As the dissolved wax reaches the cold finger surface, it precipitates, forming a layer of deposit. This process can be clearly detected in Figures 7−9: the relaxation profiles nearby the cold surface drop down very fast and the incipient deposit layer becomes visible just in 1 day after the beginning of the experiment. However, this effect appears too fast to be caused solely by growth of wax concentration. It is well-established that aggregation processes lead to the paraffin crystallization and formation of a gel-like network: as little as 0.4% of the precipitated wax[5,31] is sufficient to form a 3-D network structure of the wax crystals which behaves as a porous medium.[18,19] A considerable increase of the solid surface due to the gel network formation speeds up the relaxation considerably as it was explained above. As a result, both the increase of the local wax concentration and formation of incipient gel are the reasons for very fast decrease of relaxation times observed in the vicinity of the cold surface. Conversely, diffusion of dissolved wax molecules toward the cold wall causes wax depletion of the oil in the region $0.15 < r/r_0 < 1$, as it was established by $T_2$ profile (Figure 7).

The measurement of the deposition dynamics shows that the layers thickness grows with time in a well-known logarithmic manner (Figure 10), which has been comprehensively modeled in many papers.[7,18,19,45,46,65,66] After a certain period of time the growth almost stops, but the relaxation profiles shows that the $T_2$ values continue to decrease, Figure 7.
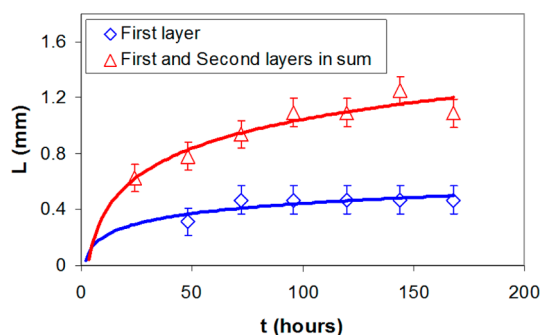


**Figure 10.** Evolution of the deposit layers thickness with time.

The well-known fact is that after a layer of wax deposit has been formed, its composition and structure gradually change with time, causing an increase of wax content, deposit hardness, melting point, etc.[5,25] This process is referred to as deposit aging. Different mechanisms of deposit aging have been elucidated; the most established are the counter diffusion[18,19,63] and Ostwald ripening,[5,67] which appear relevant for static cold finger experiment. According to the counter diffusion model, the paraffins with chain length higher than a critical carbon number (CCN) diffuse into the deposit, while the others with a length less than CCN diffuse out.[5,63] However, the distinct nature of two deposit layers observed in experiment cannot be accounted for by the aging processes only. As can be seen, there was no initial thick layer $0 < r/r_0 < 0.15$ which would be transformed into two separate ones, $0 < r/r_0 < 0.07$ and $0.07 < r/r_0 < 0.15$, during the aging; while the first of them almost reached its final thickness, the second layer just started to grow. It means that the aging processes could have occurred separately within the $0 < r/r_0 < 0.07$ region which yielded the uniform and hard deposit layer (with the shortest $T_2$ values). This observation is consistent with the model developed by Singh et al. for a relatively thin deposit layer which ages uniformly.[18] The long time of cell operating (7 days) also facilitates processes of recrystallization[5,67] which results in gel hardening: the $T_2$ value of this layer continues to decline even after the thickness stops to increase, Figure 7a. As concerning the $0.07 < r/r_0 < 0.15$ region, the aging processes there most probably occurred simultaneously with the process of deposit growing. As a result, $T_2$ values are not sharp and distributed over the layer thickness. It should be noted that formation of the branched deposit-oil boundary during growing of the outer layer is very similar to the emerging of common irregular structures during diffusion-limited aggregation processes, where the diffusion-controlled growth is predominant (some evidence of this predominance were observed in ref 68).

Temperature regime (thermal gradient) was previously shown to modulate the composition and thickness of the deposit.[18,19,69] To elucidate this effect in the cold finger cell developed, another long time experiment was carried out with the fresh portion of Mongolian oil sample: the temperature of the warm wall was the same (80 °C), but the temperature of the cold finger was set to 30 °C. The experimental procedure and cell dimensions were exactly the same as those described for the 40 °C/80 °C experiment.

The $T_2$-maps acquired during operating of the cold finger cell revealed evolution of the $T_2$-profiles in a similar way to those presented in Figure 7. The relaxation times in the vicinity of the cold wall are substantially lower than those for the rest part of the oil sample, Figure 11a; notations "4h" and "4d" correspond
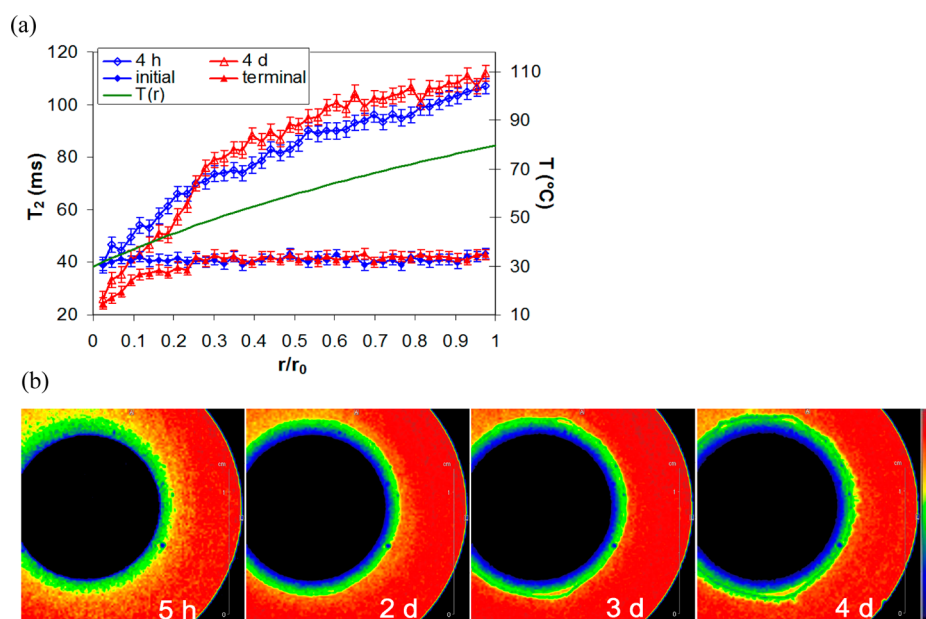
(a)



(b)



**Figure 11.** Radial $T_2$-profiles (a) and series of the $T_2$-weighted images (b) of the cold finger cell with Mongolian crude oil sample, cold/warm walls temperatures are 40/80 °C. Parameters of pulse sequence: TR = 2500 ms, TE = 40 ms.

to profiles recorded during cell operating (i.e., when $T_i = 30$ °C and $T_e = 80$ °C), while "initial" and "terminal" profiles were recorded before and after (4 days) experiment, respectively (i.e., when no temperature gradient was applied and the whole cell was at 30 °C). For convenience the T-profile (calculated according to eq 1 with assigned temperatures of the walls) is also presented in Figure 11a to show the initial temperature distribution inside the cell.

The analysis of relaxation profiles revealed appearing of the regions which have their own characteristic $T_2$ values. The first region is $0 < r/r_0 < 0.14$ with a broad distribution of $T_2 = 24-35$ ms, and the second region is $0.14 < r/r_0 < 0.25$ with a rather sharp $T_2 = 37 \pm 1$ ms (all relaxation times are inferred from "terminal" profile recorded when the heating already had been switched off). The remaining part of the oil sample, $r/r_0 > 0.25$, demonstrates characteristic $T_2 = 42 \pm 1$ ms. Taking into account considerations regarding NMR fundamentals, delineated regions $0 < r/r_0 < 0.14$ and $0.14 < r/r_0 < 0.25$ have a distinct composition and/or structure. However, by comparing the "initial" and "terminal" profiles one can conclude that these regions did not result from the considerable wax redistribution, because the remaining part of the oil experiences a very minor change in characteristic relaxation time, Figure 11a. In this case formation of the wax gel is the mechanism considered to be responsible for the apparent decrease of $T_2$.

The series of $T_2$-weighted images clearly show the process of incipient gel formation, Figure 11b. Delineated regions $0 < r/r_0 < 0.14$ with $T_2 = 24-35$ ms and $0.14 < r/r_0 < 0.25$ with $T_2 = 37 \pm 1$ ms can be attributed to different deposit layers (blue and green colors, respectively) which appears quite fast. In contrast to previous experiments where the growing incipient deposit layer can be tracked, followed by development of the second branched layer, in this experiment there is no clear point where the first layer stops to grow, giving rise to the second one. Furthermore, the evolution of the deposit layer seems primarily to occur within the thickness of incipient wax gel, and only on fourth day of experiment the first signs of branching can be noticed, Figure 11b.

According to the model developed by Singh et al., if the characteristic diffusion length of wax molecules within the deposit is comparable with the deposit thickness, the entire deposit ages uniformly.[18] Otherwise, the deposit does not age uniformly and the second layer is formed.[19] The overall thickness of the deposit increases as the temperature of cold finger decreases due to extending of the samples layer nearby the cold surface where the oil is below WAT, as it can be seen on T-profiles, Figures 7b and 11a. Consequently, the growth of thick layer is accompanied by simultaneous aging processes which lead to gradual hardening of the deposit in the vicinity of the cold surface (causing distribution of $T_2 = 24-35$ ms in $0 < r/r_0 < 0.14$ region). Decreased temperature of the cold finger makes the driving force of diffusion-controlled growth of the second branched deposit layer weaker,[19] resulting in relatively late formation of the branches.

The results obtained in this work are reliable and generally consistent with those previously reported in many studies. Numerous tests have demonstrated the same pattern of deposition processes; particularly, the two-layer structure of the deposit and its dynamics are very reproducible. No significant influence of the MRI equipment on the studied processes was observed. Moreover, application of the MRI method to more sensitive systems showed that the effects of vibrations and/or strong magnetic field on the studied systems are negligible.[40,41]

## 4. CONCLUSIONS

The cold finger cell intended for wax deposition measurements was integrated into the NMR imaging probe for the noninvasive study of the precipitation processes in situ. The implementation of the cell and test experiments with the model sample showed the stability of the operating regimes and high accuracy of the thermal gradient visualization. These encouraging results motivated further experiments with a real sample of the waxy crude oil. These experiments were focused on visualizing the precipitation processes in real oil system under static conditions and studying the deposit evolution with time

to give insight into how strong the influence of the aging processes on eventual deposit structure is.

The MRI visualization of the operating coldfinger cell revealed the formation of deposit with the morphology and dynamics strongly correlating with the temperature regime applied to the cell. When the temperature of cold surface was set relatively high (meanwhile to be lower than WAT), the incipient wax gel arose in vicinity of the cold wall, causing a substantial decrease the apparent relaxation time $T_2$. Then the thermal-driven processes of wax redistribution resulted in wax-depletion of the oil with the temperature above the WAT and formation of two wax-enriched deposit layers. The first hard layer with the lowest $T_2$ value originates from the incipient wax gel which ages uniformly due to its small thickness, while the second layer with branched structure is loosely consolidated and originates from slow diffusion-controlled deposition of wax.

The decrease of the cold wall temperature was found to facilitate extending of the deposit thickness due to the increase of the distance between the cold surface and WAT position inside the oil. Substantial decline of the apparent relaxation time $T_2$ in this case, however, was found solely due to the formation of the incipient wax gel in vicinity of the cold wall, whereas the thermal-driven wax redistribution processes appear insufficient and slow down. The relatively thick deposit layer no longer ages uniformly, and wax counter diffusion inside the deposit results in two layers with different density. The diffusion-controlled growth of branched structure was noticed relatively late as compared to the case with a higher temperature of the cold finger.

The results obtained in this study are very consistent with the majority of the data previously reported. Thus, gelation of the wax at temperatures below WAT accompanied by subsequent thermal-driven diffusion processes is considered to be a dominant mechanism of the deposit formation according to the models previously developed and validated. The counter diffusion and Ostwald ripening aging concepts were found to be relevant in the case of the cold finger study and could account for the phenomena observed in this work. We believe that the information obtained using the NMR imaging is complementary to the results obtained by other techniques which may aid in understanding the essential processes behind the wax precipitation phenomena. The approaches developed can easily be extended to study any thermal-driven phase separation processes.

## ■ AUTHOR INFORMATION

**Corresponding Authors**
*(O.N.M.) E-mail: oleg@catalysis.ru.
*(E.V.M.) E-mail: morozov_if@mil.ru.

**Notes**
The authors declare no competing financial interest.

## ■ ACKNOWLEDGMENTS

## ■ REFERENCES

(1) Bott, T. R. Aspects of Crystallization Fouling. *Exp. Therm. Fluid Sci.* **1997**, *14*, 356−360.

(2) Hughey, C. A.; Rodgers, R. P.; Marshall, A. G. Resolution of 11.000 compositionally distinct components in a single electrospray ionization Fourier transform ion cyclotron resonance mass spectrum of crude oil. *Anal. Chem.* **2002**, *74*, 4145.

(3) Simanzhenkov, V.; Idem, R. *Crude Oil Chemistry*; Marcel Dekker: New York-Basel, 2003.

(4) Mullins, O. C.; Sheu, E. Y.; Hammami, A.; Marshall, A. G. *Asphaltenes, Heavy Oils, and Petroleomics*; Springer: New York, 2007.

(5) Aiyejina, A.; Chakrabarti, D. P.; Pilgrim, A.; Sastry, M. K. S. Wax formation in oil pipelines: a critical review. *Int. J. Multiphase Flow* **2011**, *37*, 671−694.

(6) Kok, M. V.; Letoffe, J.-M.; Claudy, P.; Martin, D.; Garcin, M.; Volle, J.-L. Comparison of wax appearance temperature of crude oils by differential scanning calorimetry, thermomicroscopy and viscometry. *Fuel* **1996**, *75*, 787−790.

(7) Azevedo, L. F. A.; Teixeira, A. M. A Critical Review of the Modeling of Wax Deposition Mechanisms. *Pet. Sci. Technol.* **2003**, *21*, 393−408.

(8) Pauly, J.; Daridon, J.-L.; Sansot, J.-M.; Coutinho, J. A. P. The pressure effect on the wax formation in diesel fuel. *Fuel* **2003**, *82*, 595−601.

(9) Sarica, C.; Panacharoensawad, E. Review of paraffin deposition research under multiphase flow conditions. *Energy Fuels* **2012**, *26*, 3968−78.

(10) Srivastava, S. P.; Handoo, J.; Agrawal, K. M.; Joshi, G. C. Phase transition studies in n-alkanes and petroleum-related waxes − A review. *J. Phys. Chem. Solids* **1993**, *54*, 639.

(11) Merino-Garcia, D.; Margarone, M.; Correra, S. Kinetics of Waxy Gel Formation from Batch Experiments. *Energy Fuels* **2007**, *21*, 1287−1295.

(12) Burger, E.; Perkins, T.; Striegler, J. Studies of wax deposition in the Trans Alaska pipeline. *JPT, J. Pet. Technol.* **1981**, *33*, 1075−1086.

(13) Soedarmo, A.; Daraboina, N.; Sarica, C. Microscopic Study of Wax Deposition: Mass Transfer Boundary Layer and Deposit Morphology. *Energy Fuels* **2016**, *30*, 2674−2686.

(14) Guthrie, S. E.; Mazzanti, G.; Steer, T. N.; Stetzer, M. R.; Kautsky, S. P.; Merz, H.; Idziak, S. H. J.; Sirota, E. B. An in situ method for observing wax crystallization under pipe flow. *Rev. Sci. Instrum.* **2004**, *75*, 873−877.

(15) Soedarmo, A. A.; Daraboina, N.; Lee, H. S.; Sarica, C. Microscopic Study of Wax Precipitation-Static Conditions. *Energy Fuels* **2016**, *30*, 954−961.

(16) Zougari, M. I. Shear driven crude oil wax deposition evaluation. *J. Pet. Sci. Eng.* **2010**, *70*, 28−34.

(17) Huang, Z.; Lu, Y.; Hoffmann, R.; Amundsen, L.; Fogler, H. S. The Effect of Operating Temperatures on Wax Deposition. *Energy Fuels* **2011**, *25*, 5180−5188.

(18) Singh, P.; Venkatesan, R.; Fogler, H. S.; Nagarajan, N. R. Formation and aging of insipient thin film wax-oil gels. *AIChE J.* **2000**, *46*, 1059.

(19) Singh, P.; Venkatesan, R.; Fogler, H. S.; Nagarajan, N. R. Morphological Evolution of Thick Wax Deposits during Aging. *AIChE J.* **2001**, *47*, 6−18.

(20) Hoffmann, R.; Amundsen, L. Single-phase wax deposition experiments. *Energy Fuels* **2010**, *24*, 1069−80.

(21) Castillo, J.; Canelon, C.; Acevedo, S.; Carrier, H.; Daridon, J.-L. Optical fiber extrinsic refractometer to measure RI of samples in a high pressure and temperature systems: Application to wax and asphaltene precipitation measurements. *Fuel* **2006**, *85*, 2220−2228.

(22) Polacco, G.; Filippi, S.; Paci, M.; Giuliani, F.; Merusi, F. Structural and rheological characterization of wax modified bitumens. *Fuel* **2012**, *95*, 407−416.

(23) Matzain, A.; Apte, M. S.; Zhang, H.-Q.; Volk, M.; Brill, J. P.; Creek, J. L. Investigation of Paraffin Deposition During Multiphase Flow in Pipelines and Wellbores—Part 1: Experiments. *J. Energy Resour. Technol.* **2002**, *124*, 180−186.

(24) Halstensen, M.; Arvoh, B. K.; Amundsen, L.; Hoffmann, R. Online estimation of wax deposition thickness in single-phase sub-sea pipelines based on acoustic chemometrics: A feasibility study. *Fuel* **2013**, *105*, 718−727.

(25) Creek, J. L.; Lund, H. J.; Brill, J. P.; Volk, M. Wax deposition in single phase flow. *Fluid Phase Equilib.* **1999**, *158-160*, 801−811.

(26) Jiang, Z.; Hutchinson, J. M.; Imrie, C. T. Measurement of the wax appearance temperatures of crude oils by temperature modulated differential scanning calorimetry. *Fuel* **2001**, *80*, 367−371.

(27) Hoffmann, R.; Amundsen, L.; Schuller, R. Online monitoring of wax deposition in sub-sea pipelines. *Meas. Sci. Technol.* **2011**, *22*, 075701.

(28) Mei, I. L. S.; Ismail, I.; Shafquet, A.; Abdullah, B. Real-time monitoring and measurement of wax deposition in pipelines via non-invasive electrical capacitance tomography. *Meas. Sci. Technol.* **2016**, *27*, 025403.

(29) Coto, B.; Martos, C.; Pena, J. L.; Espada, J. J.; Robustillo, M. D. A new method for the determination of wax precipitation from non-diluted crude oils by fractional precipitation. *Fuel* **2008**, *87*, 2090−2094.

(30) Schabron, J. F.; Rovani, J. F.; Sanderson, M. M.; Loveridge, J. L.; Nyadong, L.; McKenna, A. M.; Marshall, A. G. Waxphaltene Determinator Method for Automated Precipitation and Redissolution of Wax and Asphaltene Components. *Energy Fuels* **2012**, *26*, 2256−2268.

(31) Paso, K.; Senra, M.; Yi, Y.; Sastry, A. M.; Fogler, H. S. Paraffin polydispersity facilitates mechanical gelation. *Ind. Eng. Chem. Res.* **2005**, *44*, 7242−7254.

(32) Masoudi, Sh.; Vafaie Sefti, M.; Jafari, H.; Modares, H. The Hardening Process and Morphology of a Wax Deposit in a Pipe Flow. *Pet. Sci. Technol.* **2010**, *28*, 1598−1610.

(33) Tian, Z.; Jin, W.; Wang, L.; Jin, Z. The study of temperature profile inside wax deposition layer of waxy crude oil in pipeline. *Front. Heat Mass Transfer* **2014**, *5*, 1−8.

(34) Trukhan, S. N.; Yudanov, V. F.; Gabrienko, A. A.; Subramani, V.; Kazarian, S. G.; Martyanov, O. N. In Situ Electron Spin Resonance Study of Molecular Dynamics of Asphaltenes at Elevated Temperature and Pressure. *Energy Fuels* **2014**, *28*, 6315−6321.

(35) Gabrienko, A. A.; Martyanov, O. N.; Kazarian, S. G. Effect of Temperature and Composition on the Stability of Crude Oil Blends Studied with Chemical Imaging In Situ. *Energy Fuels* **2015**, *29*, 7114−7123.

(36) Gabrienko, A. A.; Subramani, V.; Martyanov, O. N.; Kazarian, S. G. Correlation between Asphaltene Stability in n-Heptane and Crude Oil Composition Revealed with In Situ Chemical Imaging. *Adsorpt. Sci. Technol.* **2014**, *32*, 243−255.

(37) Blumich, B. *NMR Imaging of Materials*; Clarendon Press: Oxford, 2003.

(38) Stapf, S.; Han, S.-I. *NMR Imaging in Chemical Engineering*; Wiley-VCH: Weinheim, 2006.

(39) Mitchell, J.; Chandrasekera, T. C.; Holland, D. J.; Gladden, L. F.; Fordham, E. J. Magnetic Resonance Imaging in Laboratory Petrophysical Core Analysis. *Phys. Rep.* **2013**, *526*, 165−225.

(40) Gabrienko, A. A.; Morozov, E. V.; Subramani, V.; Martyanov, O. N.; Kazarian, S. G. Chemical Visualization of Asphaltenes Aggregation Processes Studied in Situ with ATR-FTIR Spectroscopic Imaging and NMR Imaging. *J. Phys. Chem. C* **2015**, *119*, 2646−2660.

(41) Morozov, E. V.; Martyanov, O. N. Probing Flocculant-Induced Asphaltene Precipitation via NMR Imaging: from Model Toluene-Asphaltene Systems to Natural Crude Oils. *Appl. Magn. Reson.* **2016**, *47*, 223−235.

(42) Chala, G. T.; Sulaiman, S. A.; Japper-Jaafar, A.; Wan Abdullah, W. A. K. Effects of cooling regime on the formation of voids in statically cooled waxy crude oil. *Int. J. Multiphase Flow* **2015**, *77*, 187−195.

(43) Mendes, R.; Vinay, G.; Ovarlez, G.; Coussot, P. Reversible and irreversible destructuring flow in waxy oils: An MRI study. *J. Non-Newtonian Fluid Mech.* **2015**, *220*, 77−86.

(44) Dos Santos, J. S. T.; Fernandes, A. C.; Giulietti, M. Study of the paraffin deposit formation using the cold finger methodology for Brazilian crude oils. *J. Pet. Sci. Eng.* **2004**, *45*, 47−60.

(45) Correra, S.; Fasano, A.; Fusi, L.; Primicerio, M. Modelling wax diffusion in crude oils: The cold finger device. *Appl. Math. Modelling* **2007**, *31*, 2286−2298.

(46) Correra, S.; Fasano, A.; Fusi, L.; Primicerio, M.; Rosso, F. Wax diffusivity under given thermal gradient: a mathematical model. *Z. Angew. Math. Mech.* **2007**, *87*, 24−36.

(47) Kasumu, A. S.; Mehrotra, A. K. Solids Deposition from Wax−Solvent−Water "Waxy" Mixtures Using a Cold Finger Apparatus. *Energy Fuels* **2015**, *29*, 501−511.

(48) Paso, K. G.; Fogler, H. S. Influence of n-paraffin composition on the aging of wax−oil gel deposits. *AIChE J.* **2003**, *49*, 3241−3251.

(49) Quan, Q.; Gong, J.; Wang, W.; Gao, G. Study on the aging and critical carbon number of wax deposition with temperature for crude oils. *J. Pet. Sci. Eng.* **2015**, *130*, 1−5.

(50) Jennings, D. W.; Weispfennig, K. Effects of shear and temperature on wax deposition: coldfinger investigation with a Gulf of Mexico Crude Oil. *Energy Fuels* **2005**, *19*, 1376−1386.

(51) Golovko, A. K.; Gorbunova, L. V.; Kam'yanov, V. F. The regularities in the structural group composition of high-molecular heteroatomic petroleum components. *Russian Geology and Geophysics* **2010**, *51*, 286−295.

(52) Golovko, A. K.; Gorbunova, L. V.; Kam'yanov, V. F.; Murneren, T. M.; Ogorodnikov, V. D. Chemical group composition of oils from eastern and southeastern Mongolia. *Pet. Chem.* **2004**, *44*, 238−245.

(53) Nemirovskaya, G. B.; Emel'yanova, A. S.; Ashmyan, K. D. Methods of Analysis of High-Wax Crude Oils. Resins, Asphaltenes, Paraffin Waxes. *Chem. Technol. Fuels Oils* **2005**, *41*, 236−240.

(54) *ASTM D6560, Standard Test Method for Determination of Asphaltenes (Heptane Insolubles) in Crude Petroleum and Petroleum Products*; ASTM International: West Conshohocken, PA, 2012; http://www.astm.org/Standards/D6560.htm.

(55) *ASTM D97, Standard Test Method for Pour Point of Petroleum Products*; ASTM International: West Conshohocken, PA, 2016; http://www.astm.org/Standards/D97.htm.

(56) Coutinho, J. A. P.; Daridon, J.-L. The Limitations of the Cloud Point Measurement Techniques and the Influence of the Oil Composition on Its Detection. *Pet. Sci. Technol.* **2005**, *23*, 1113−1128.

(57) *ASTM D7042−16e1, Standard Test Method for Dynamic Viscosity and Density of Liquids by Stabinger Viscometer (and the Calculation of Kinematic Viscosity)*; ASTM International: West Conshohocken, PA, 2016; http://www.astm.org/Standards/D7042.htm.

(58) Shirchin, B.; Nordov, E.; Monkhoobor, D.; Sainbayar, A. Study on Main Physical and Chemical Characteristics of East Mongolian Petroleum. *J. Ind. Eng. Chem.* **2003**, *14*, 423−425.

(59) Tugsuu, T.; Yoshikazu, S.; Enkhsaruul, B.; Monkhoobor, D. A Comparative Study on the Hydrocracking for Atmospheric Residue of Mongolian Tamsagbulag Crude Oil and Other Crude Oils. *Adv. Chem. Eng. Sci.* **2012**, *2*, 402−407.

(60) Callaghan, P. *Principles of Nuclear Magnetic Resonance Microscopy*; Clarendon Press: Oxford, 1993.

(61) Levitt, M. H. *Spin Dynamics: Basics of Nuclear Magnetic Resonance*, 2nd ed.; John Wiley & Sons: Southampton, 2007.

(62) Bernstein, M. A.; King, K. F.; Zhou, X. J. *Handbook of MRI Pulse Sequences*; Elsevier Academic Press: Burlington, 2004.

(63) Singh, P.; Youyen, A.; Fogler, H. S. Existence of a Critical Carbon Number in the Aging of a Wax-Oil Gel. *AIChE J.* **2001**, *47*, 2111−2124.

(64) Bloembergen, N.; Purcell, E. M.; Pound, R. V. *Phys. Rev.* **1948**, *73*, 679.

(65) Eskin, D.; Ratulowski, J.; Akbarzadeh, K. A. A model of wax deposit layer formation. *Chem. Eng. Sci.* **2013**, *97*, 311−319.

(66) Fasano, A.; Fusi, L.; Correra, S.; Margarone, M. A Survey on Mathematical Modelling of Deposition in Waxy Crude Oils. *Math. Modell. Nat. Phenom.* **2011**, *6*, 157−183.

(67) Coutinho, J. A. P.; Lopes-da-Silva, J. A.; Ferreira, A.; Rosario Soares, M. R.; Daridon, J.-L. (2003) Evidence for the Aging of Wax Deposits in Crude Oils by Ostwald Ripening. *Pet. Sci. Technol.* **2003**, *21*, 381−391.

(68) Lopes-da-Silva, J. A.; Coutinho, J. A. P. Analysis of the Isothermal Structure Development in Waxy Crude Oils under Quiescent Conditions. *Energy Fuels* **2007**, *21*, 3612−3617.

(69) Paso, K. G.; Fogler, H. S. Bulk stabilization in wax deposition systems. *Energy Fuels* **2004**, *18*, 1005−1013.